Coherent Dynamics of Coupled Electron and Nuclear Spin Qubits in Diamond

L. Childress, *et al.*

Science **314**, 281 (2006);
DOI: 10.1126/science.1131871

Science (print ISSN 0036-8075; online ISSN 1095-9203) is published weekly, except the last week in December, by the American Association for the Advancement of Science, 1200 New York Avenue NW, Washington, DC 20005.

with experiment, and although the polarizabilities of the (relativistic) IBr states are difficult to calculate (*30*), DSC will always be possible if there are differential polarizabilities between states.

We have shown that the nonresonant dynamic Stark effect can be used to dynamically alter a potential energy barrier in a photochemical reaction, promoting the formation of a given product. Variants of DSC that incorporate Raman pumping will be applicable to ground-state reactions. Pulse-shaping methods from the quantum control toolbox will also prove useful. For example, implementing DSC with adaptive-feedback techniques will lead to the design of custom-shaped Stark-control laser pulses. As well, it will be possible to use interference effects in DSC to alter, for example, excited-state lifetimes (*29*). The frequency independence, the avoidance of excited state chemistry, and the universal applicability of the nonresonant dynamic Stark effect should prove important for scaling DSC to larger and more complex systems.

References and Notes

1. P. W. Brumer, M. Shapiro, *Principles of the Quantum Control of Molecular Processes* (Wiley-Interscience, Hoboken, NJ, 2003).
2. S. A. Rice, M. Zhao, *Optical Control of Molecular Dynamics* (Wiley, New York, 2000).
3. A. D. Bandrauk, Ed., *Molecules in Laser Fields* (Marcel Dekker, New York, 1994).
4. H. Rabitz, *Science* **299**, 525 (2003).
5. H. Rabitz, R. de Vivie-Riedle, M. Motzkus, K. Kompa, *Science* **288**, 824 (2000).
6. L. J. Frasinski *et al.*, *Phys. Rev. Lett.* **58**, 2424 (1987).
7. C. Cornaggia, J. Lavancier, D. Normand, J. Morellec, H. X. Liu, *Phys. Rev. A* **42**, 5464 (1990).
8. M. Lezius *et al.*, *Phys. Rev. Lett.* **86**, 51 (2001).
9. H. Niikura, P. B. Corkum, D. M. Villeneuve, *Phys. Rev. Lett.* **90**, 203601 (2003).
10. R. S. Judson, H. Rabitz, *Phys. Rev. Lett.* **68**, 1500 (1992).
11. A. Assion *et al.*, *Science* **282**, 919 (1998).
12. R. J. Levis, G. M. Menkir, H. Rabitz, *Science* **292**, 709 (2001); published online 29 March 2001 (10.1126/science.1059133).
13. M. Shapiro, Y. Zeiri, *J. Chem. Phys.* **85**, 6449 (1986).
14. A. Vardi, M. Shapiro, *Phys. Rev. A* **58**, 1352 (1998).
15. T. F. George, J.-M. Yuan, I. H. Zimmerman, J. R. Laing, *Faraday Discuss. Chem. Soc.* **62**, 246 (1977).
16. W. Domcke, D. R. Yarkony, H. Koeppel, Eds., *Conical Intersections: Electronic Structure, Dynamics, and Spectroscopy* (World Scientific, Singapore, 2004).
17. M. Child, *Mol. Phys.* **32**, 1495 (1976).
18. C. K. Chan, P. Brumer, M. Shapiro, *J. Chem. Phys.* **94**, 2688 (1991).
19. P. Gross, D. B. Bairagi, M. K. Mishra, H. Rabitz, *Chem. Phys. Lett.* **223**, 263 (1994).
20. R. R. Garcia, S. Solomon, *J. Geophys. Res.* **99**, 12937 (1994).
21. R. Vogt, R. Sander, R. von Glasow, P. J. Crutzen, *J. Atmos. Chem.* **32**, 375 (1999).
22. The 1-kHz laser system consists of a Ti:Sapphire oscillator pumping a regenerative amplifier. The 800-nm output pumps a pair of optical parametric amplifiers (OPAs). The idler output from OPA1 (1730 nm) was used for the control pulse, whereas the signal (1485 nm) was mixed with residual 800-nm light to produce the 520-nm pump wavelength. The signal beam from OPA2 (1218 nm) was doubled and then doubled again to make the 304.5-nm ultraviolet (UV) probe. The REMPI probe is bandwidth-narrowed by use of long doubling crystals to ensure high selectivity. Telescopes were used to expand the three beams to varying diameters such that the focal-spot size ratios at the interaction region were UV:visible:IR = 1:1.5:2. Careful co-collimation then assured that the IR field was sampled at a uniform intensity.
23. A. T. J. B. Eppink, D. H. Parker, *Rev. Sci. Instrum.* **68**, 3477 (1997).
24. E. Wrede *et al.*, *J. Chem. Phys.* **114**, 2629 (2001).
25. B. W. Shore, *The Theory of Coherent Atomic Excitation*, vols. I and II (Wiley, New York, 1990).
26. B. J. Sussman, J. G. Underwood, R. Lausten, M. Y. Ivanov, A. Stolow, *Phys. Rev. A* **73**, 053403 (2006).
27. C. Y. Zhu, Y. Teranishi, H. Nakamura, *Adv. Chem. Phys.* **117**, 127 (2001).
28. M. Shapiro, H. Bony, *J. Chem. Phys.* **83**, 1588 (1985).
29. B. J. Sussman, M. Y. Ivanov, A. Stolow, *Phys. Rev. A* **71**, 051401 (2005).
30. S. Patchkovskii, *Phys. Chem. Chem. Phys.* **8**, 926 (2006).

31. We thank P. Corkum and M. Shapiro for many useful discussions and R. Lausten, R. Bhardwaj, and D. Rayner for their assistance with the experiment.

10 July 2006; accepted 23 August 2006
10.1126/science.1132289

Coherent Dynamics of Coupled Electron and Nuclear Spin Qubits in Diamond

L. Childress,[1]* M. V. Gurudev Dutt,[1]* J. M. Taylor,[1] A. S. Zibrov,[1] F. Jelezko,[2] J. Wrachtrup,[2] P. R. Hemmer,[3] M. D. Lukin[1]†

Understanding and controlling the complex environment of solid-state quantum bits is a central challenge in spintronics and quantum information science. Coherent manipulation of an individual electron spin associated with a nitrogen-vacancy center in diamond was used to gain insight into its local environment. We show that this environment is effectively separated into a set of individual proximal ^{13}C nuclear spins, which are coupled coherently to the electron spin, and the remainder of the ^{13}C nuclear spins, which cause the loss of coherence. The proximal nuclear spins can be addressed and coupled individually because of quantum back-action from the electron, which modifies their energy levels and magnetic moments, effectively distinguishing them from the rest of the nuclei. These results open the door to coherent manipulation of individual isolated nuclear spins in a solid-state environment even at room temperature.

The controlled, coherent manipulation of quantum-mechanical systems is an important challenge in modern science and engineering (*1*). Solid-state quantum systems such as electronic spins (*2*–*10*), nuclear spins (*11*, *12*), and superconducting islands (*13*) are among the most promising candidates for realization of qubits. However, in contrast to isolated atomic systems (*14*), these solid-state qubits couple to a complex environment, which often leads to rapid loss of coherence and, in general, is difficult to understand (*15*–*19*).

We used spin-echo spectroscopy on a single-electron solid-state qubit to gain insight into its local environment. We investigated a single nitrogen-vacancy (NV) center in a high-purity diamond sample and showed that its electron spin coherence properties are determined by ^{13}C nuclear spins. Most importantly, we demonstrated that the electron spin couples coherently to individual proximal ^{13}C spins. By selecting an NV center with a desired nearby ^{13}C nucleus and adjusting the external magnetic field, we could effectively control the coupled electron-nuclear spin system. Our results show that it is possible to coherently address individual isolated nuclei in the solid state and manipulate them via a nearby electron spin. Because of the long coherence times of isolated nuclear spins (*20*), this is an important element of many solid-state quantum information approaches from quantum computing (*11*, *12*) to quantum repeaters (*21*, *22*).

Spin echo is widely used in bulk electron spin resonance (ESR) experiments to study interactions and to determine the structure of complex molecules (*23*). Recently, local contact interactions were observed between single-NV electronic spins and the nuclear spins associated with the host nitrogen and the nearest-neighbor carbon atoms (*3*, *24*). In the latter case, coherent dynamics of electron and nuclear spins were observed (*3*). We show that coherent coupling extends to separated isolated nuclei, which nominally constitute the electron environment and couple weakly to the electron spin.

The NV center stands out among solid-state systems because its electronic spin can be efficiently prepared, manipulated, and measured with optical and microwave excitation (*2*). The electronic ground state of the NV center is a spin triplet that exhibits a 2.87-GHz zero-field splitting, defining the $\hat{z}$ axis of the electron spin (Fig. 1A). Application of a small magnetic field splits the magnetic sublevels $m_s = \pm 1$, allowing selective microwave excitation of a single spin transition.

Our observations can be understood by considering how the NV electron spin interacts

[1]Department of Physics and Institute for Quantum Science and Engineering, Harvard University, Cambridge, MA 02138, USA. [2]Physikalisches Institut, Universitat Stuttgart, Pfaffenwaldring 57 D-70550 Stuttgart, Germany. [3]Department of Electrical and Computer Engineering, Texas A&M University, College Station, TX 77843, USA.

*These authors contributed equally to this work.
†To whom correspondence should be addressed. E-mail: lukin@fas.harvard.edu

with a proximal spin-½ nucleus in the diamond lattice. If the electron spin is in the state with zero magnetic moment (m_s = 0), it does not interact with the nuclear spin, which is thereby free to precess under the influence of a small magnetic field applied externally. However, if the electron is in either of the m_s = ±1 states, then it generates a large local magnetic field that inhibits the free precession of nearby nuclei (*25*, *26*). Hence, the nuclear precession is conditional on the state of the electron. In particular, if the electron spin is prepared in a superposition state, then it becomes entangled with the nuclear spins at a rate determined by the external magnetic field, i.e., the Larmor frequency. In practice, the diamond lattice contains a large number of randomly placed nuclear spins. The electron becomes entangled with all of them and thus decoheres on the time scale of the Larmor period. Coherent coupling to individual proximal nuclear spins is nevertheless possible, because the electron spin effectively enhances their magnetic susceptibilities and hence their precession frequency.

In our experiments, single NV centers were isolated and addressed at room temperature by using optical scanning confocal microscopy (Fig. 1B) with excitation at 532 nm and fluorescence detection over the range from 650 to 800 nm. Each circled spot is a single NV center, which was verified by photon correlation measurements (inset). We investigated over 20 individual centers in detail, and where relevant we indicate which center we observed. The 532-nm excitation polarizes the spin triplet into the m_s = 0 state on the time scale of a few microseconds. After microwave manipulation of the spin, we detected the remaining population in the m_s = 0 state by again applying the excitation laser. Just after the 532-nm light is applied, the m_s = 0 state fluoresces more strongly than the m_s = ±1 states, allowing measurement of the spin (Fig. 1C) (*27*). Oscillations in fluorescence occur as a function of the duration of a microwave pulse resonant with the m_s = 0 to m_s = 1 transition (*2*) (Fig. 1D). These Rabi nutations should correspond to complete population transfer within the two-state system. Fluorescence data were thus normalized in units of m_s = 0 probability, p, where p = 1 and p = 0 correspond to the maximum and the minimum fluorescence, respectively, in a fit to Rabi oscillations observed under the same conditions.

To probe coherence properties of single electron spins, we make use of Ramsey spectroscopy and spin echo techniques (*28*). The free electron spin precession [Ramsey signal (*28*)] dephases on a fast time scale, T_2^* = 1.7 ± 0.2 μs (Fig. 1E). Moreover, the signal exhibits a complex oscillation pattern caused by level shifts from the host ^{14}N nucleus and other nearby spins (*27*). These frequency shifts can be eliminated by using a spin-echo (or Hahn echo) technique (*29*). It consists of the sequence $\pi/2 - \tau - \pi - \tau' - \pi/2$, where π represents a microwave pulse of sufficient duration to flip the electron spin from m_s = 0 to m_s = 1 and τ and τ' are durations of free precession intervals. When the two wait times are equal, $\tau = \tau'$, this sequence decouples the spin from an environment that changes slowly compared with τ (Fig. 2A). Decay of a typical Hahn echo signal (Fig. 2B) yielded a much longer coherence time, $\tau_C \approx 13 \pm 0.5\ \mu s \gg T_2^*/2$, thus indicating a long correlation (memory) time associated with the electron spin environment.

Spin-echo spectroscopy provides a useful tool for understanding this environment: By observing the spin-echo signal under varying conditions, we can indirectly determine the response of the environment and, from this, glean details about the environment itself. In particular, we observe that the echo signal depends on the magnetic field. As the magnetic field is increased, the initial decay of the spin echo signal occurs faster and faster. However, the signal revives at longer times, when τ equals τ_R (*30*). Figure 2C shows a typical spin-echo signal (center B) in moderate magnetic field as a function of time ($\tau = \tau'$). The initial collapse of the signal is followed by periodic revivals extending out to $2\tau \sim 240$ μs. We find that the revival rate, $1/\tau_R$, precisely matches the Larmor precession frequency for ^{13}C nuclear spins of 1.071 kHz/G (Fig. 3A). This result indicates that the dominant environment of the NV electron spin is a nuclear spin bath formed by the spin-½ ^{13}C isotope, which exists in 1.1% abundance in the otherwise spinless ^{12}C diamond lattice (Fig. 3B). The ^{13}C precession induced periodic decorrelation and rephasing of the nuclear spin bath, which led to collapses and revivals of the electron spin-echo signal (Fig. 2C).

Every NV center studied exhibited spin-echo collapse and revival on long time scales, but many also showed more complicated evolution on short time scales. As an example, the spin-echo signal from NV center E (Fig. 4A) showed oscillations with slow and fast components at ~0.6 MHz and ~9 MHz, respectively. The fast component (referred to as the modulation frequency) was relatively insensitive to the magnetic field (Fig. 4B), but the slow component (envelope frequency) varied dramatically with the magnetic field amplitude and orientation (Fig. 4, C and D). These observations indicate that the electron spin gets periodically entangled and disentangled with an isolated system until the spin echo finally collapses from interactions with the precessing bulk spin bath. Although the data are not shown, some NV centers, for example NV C, exhibited several envelope and modulation

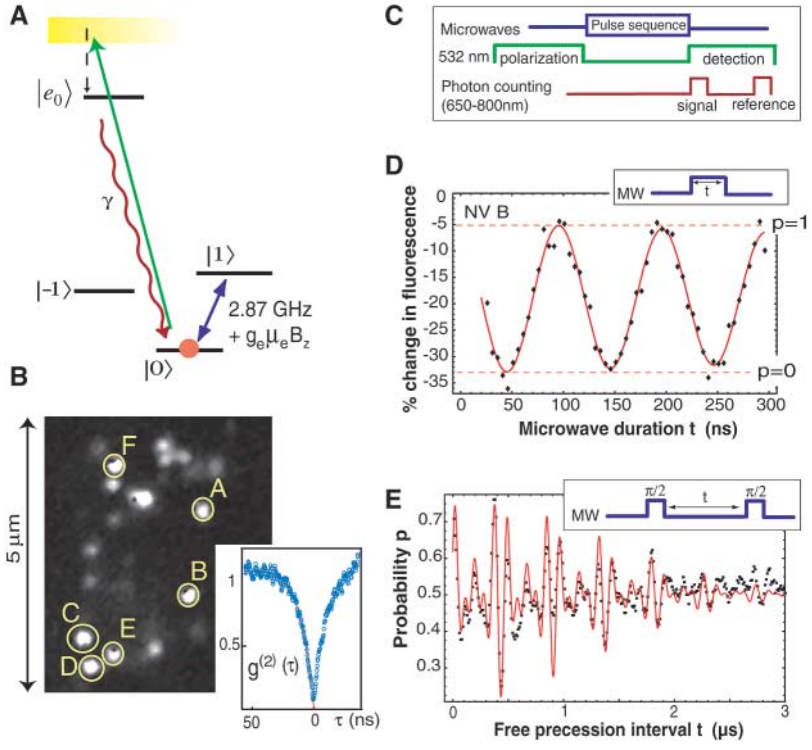

Fig. 1. (**A**) The energy level structure of the NV center. (**B**) Scanning confocal image showing locations of single NV centers A to F. (Inset) A representative measured auto-correlation function $g^{(2)}(\tau)$ from a single NV center, where $g^{(2)}(0) \ll$ ½ indicates that we are exciting a single quantum emitter. (**C**) Experimental procedure. (**D**) Driven spin oscillations (Rabi nutations). The percent change in fluorescence between the signal and reference is observed as a function of resonant microwave (MW) pulse duration (inset) for NV center B. (**E**) Electron-spin free precession. The data were taken with a microwave detuning of 8 MHz as a function of delay between the two $\pi/2$ pulses (inset). The Ramsey signal was fitted (red) to $\exp[-(t/T_2^*)^2]\sum_{i=1}^{3}\cos(2\pi f_i t)$, where f_i values correspond to the level shifts from the host ^{14}N nuclear spin, obtaining $T_2^* = 1.7 \pm 0.2$ μs.

frequencies, indicating that the electron spin interacts coherently with multiple ^{13}C nuclei. Other centers, for example NV F, showed no evidence of proximal ^{13}C spins.

To provide a quantitative explanation for these results, we first considered the spin-echo signal arising from a single ^{13}C nucleus $\mathbf{I}^{(j)}$ located a distance r_j in the direction $\mathbf{n}_j$ from the NV spin. This ^{13}C spin couples to the electron spin via the hyperfine interaction (*23*, *31*):

$$V^{(j)} = -\mu_e\mu_n \frac{8\pi|\psi_e(r_j)|^2}{3}\mathbf{S}\cdot\mathbf{I}^{(j)} + \left\langle \frac{\mu_e\mu_n}{r_j^3}\left\{\mathbf{S}\cdot\mathbf{I}^{(j)} - 3[\mathbf{n}_j\cdot\mathbf{S}][\mathbf{n}_j\cdot\mathbf{I}^{(j)}]\right\}\right\rangle \quad (1)$$

where μ_e and μ_n are the electron and nuclear magnetic moments, respectively, $|\psi_e(r_j)|^2$ is the electron spin density at the site of the nuclear spin, and angle brackets denote an average over the electron wavefunction, $\psi_e(r)$. The essence of this Hamiltonian, which can be represented as $V^{(j)} = \mathbf{B}^{(j)}_{ms}\cdot\mathbf{I}^{(j)}$, is that the nuclear spin experiences an effective magnetic field, $\mathbf{B}^{(j)}_{ms}$, that depends on the electron spin state m_s. This electron spin state–dependent magnetic field leads to conditional evolution of the nuclear spin, thereby entangling the two spins. Because of the spatial dependence of the hyperfine interaction, these effects decrease rapidly with distance from the NV center, making proximal nuclei stand out from the remainder of the spin bath.

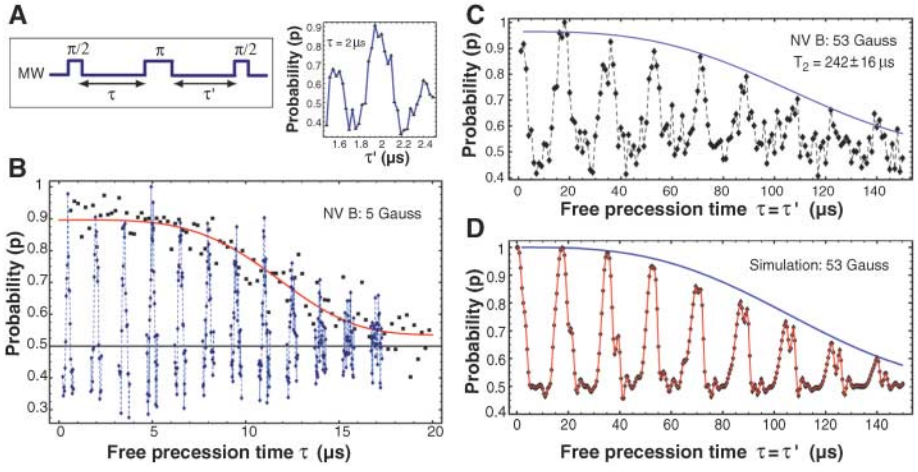

Fig. 2. (**A**) Spin echo. The spin-echo pulse sequence (left) is shown along with a representative time-resolved spin echo (right) from NV center B. A single spin echo is observed by holding τ fixed and varying τ'. (**B**) Spin echo decay for NV center B in a small magnetic field (B ~ 5 G). Individual echo peaks are mapped out by scanning τ' for several values of τ (blue curves). The envelope for the spin echoes (black squares), which we refer to as the spin-echo signal, maps out the peaks of the spin echoes. It is obtained by varying τ and τ' simultaneously so that $\tau = \tau'$ for each data point. The spin-echo signal is fitted to $\exp[-(\tau/\tau_c)^4]$ (red curve) to obtain the estimated coherence time $\tau_c = 13 \pm 0.5$ μs. (**C**) Collapse and revival of the spin-echo signal from NV center B in a moderate magnetic field (53 G). The decay of the revivals (blue curve) is found by fitting the height of each revival to $\exp[-(2\tau/T_2)^3]$, as would be expected from ^{13}C dipole-dipole induced dephasing (*24*, *31*), with $T_2 \approx 242 \pm 16$ μs. (**D**) Simulation of collapse and revival for an NV center in 53 G applied magnetic field, surrounded by a random distribution of 1.1% ^{13}C spins (*27*). Additional structure in the simulation arises from coherent interactions with the nearest ^{13}C in the lattice, via the same mechanism shown in Fig. 4. The phenomenological decay is added to the simulation for comparison with experimental data.

The hyperfine interaction between the electron spin and a single nuclear spin has a dramatic effect on the spin-echo signal. After the initial $\pi/2$ pulse in the spin-echo sequence, the electron spin state $(|m_s = 0\rangle + |m_s = 1\rangle)/\sqrt{2}$ becomes entangled with the nuclear spin state at a rate determined by $\mathbf{B}^{(j)}_0$ and $\mathbf{B}^{(j)}_1$. As the electron spin becomes entangled with the nuclear spin, the spin-echo signal diminishes; when it gets disentangled, the signal revives. The resulting spin-echo signal thus exhibits periodic reductions in amplitude, with modulation frequencies $\omega_{j,ms}$ associated with each spin-dependent field $\mathbf{B}^{(j)}_{ms}$. By considering the unitary evolution associated with the dipole Hamiltonian [see, e.g., (*26*) for derivation], we obtained a simple expression for the spin echo signal, $p_j = (S_j + 1)/2$, with pseudospin S_j given by

$$S_j(\tau) = 1 - \frac{2|\mathbf{B}_0^{(j)} \times \mathbf{B}_1^{(j)}|^2}{|B_0^{(j)}|^2|B_1^{(j)}|^2} \times \sin^2(\omega_{j,0}\tau/2)\sin^2(\omega_{j,1}\tau/2) \quad (2)$$

Because the electron spin dipole field is stronger for $m_s = 1$, we associated $\omega_{j,1}$ with the fast modulation frequency and $\omega_{j,0}$ with the slower envelope frequency. Furthermore, we included multiple ^{13}C nuclei in our description by taking a sum over the dipole interactions, $V = \sum_j V^{(j)}$; the corresponding unitary evolution yields the echo signal $p = (S + 1)/2$ with $S = \prod_j S_j$.

We began with a simple treatment, which neglected the terms proportional to S_x and S_y because they are suppressed by the large electron-spin splitting $\Delta \approx 2.87$ GHz [the so-called secular approximation (*23*)]. In this model (Fig. 3C), the $m_s = 1$ nuclear-spin states have a fixed hyperfine splitting, $\omega_{j,1} \sim \mu_e\mu_n[\langle 1/r_j^3\rangle + 8\pi|\Psi_e(r_j)|^2/3]$, whereas the degenerate $m_s = 0$ nuclear-spin states can precess in a small applied magnetic field at the bare ^{13}C Larmor frequency $\omega_{j,0} = \omega_0$. When we included many nuclear spins in the echo signal, the fast echo modulations $\omega_{j,1}$ interfered with each other, causing initial decay of the signal as $\exp-(\tau/\tau_c)^4$. However, when $\tau = \tau' = 2\pi/\omega_0$, S_j equaled 1

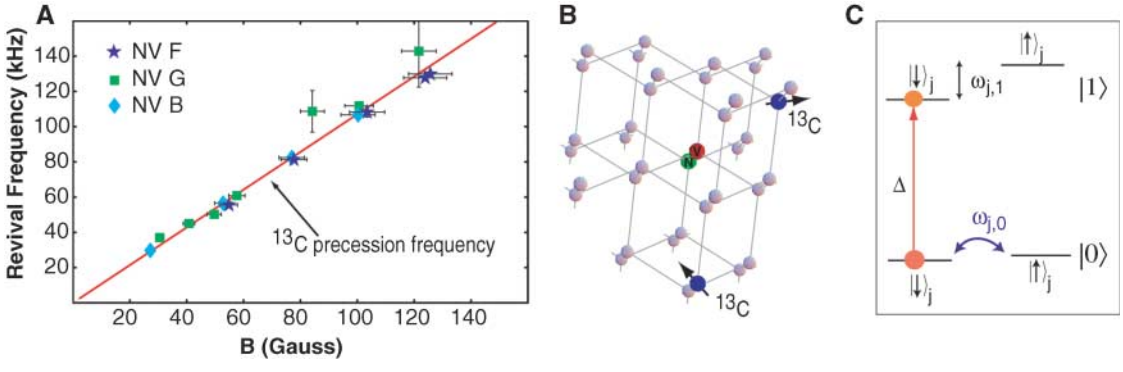

Fig. 3. (**A**) Spin-echo revival frequency as a function of magnetic field amplitude. Data from three representative centers—NV B, NV F, and NV G (not shown in Fig. 1B)—exhibit revivals that occur with the ^{13}C Larmor precession frequency (red). The data points for NV centers B and F were taken with $B \| \hat{z}$, whereas the data for NV center G were taken in a variety of magnetic field orientations. (**B**) Illustration of the ^{13}C environment surrounding the NV center. (**C**) Physical model for spin-echo modulation.

for all j, and the spin-echo signal revived. Simulations based on Eqs. 1 and 2 (Fig. 2D) are in good agreement with the observed collapses and revivals.

Such a simple picture cannot explain the observed echo modulation, however, because it predicts that the spin-echo signal should collapse before coherent interactions with individual ^{13}C spins become visible. In fact, the nonsecular terms in the Zeeman and dipole interactions slightly mix the electron-spin levels, introducing some electronic character to the nearby nuclear-spin levels and thus augmenting their magnetic moment by $\sim\mu_e(\omega_{j,1}/\Delta)$. Because $\mu_e \gg \mu_n$, this greatly enhances the nuclear Larmor precession rate for nearby spins. Furthermore, the enhancement is anisotropic: It is strongest when the external field is oriented perpendicular to the NV axis, corresponding to the largest degree of mixing. For a properly oriented magnetic field, proximal nuclei can thereby entangle and disentangle with the NV spin on time scales much faster than the bare ^{13}C Larmor period.

These theoretical predictions are in good agreement with our observations (Fig. 4). In addition, by fitting the envelope frequency as a function of magnetic field, we were able to estimate the six coupling parameters that characterize the hyperfine interaction (*27*). In principle, these parameters should also allow for precise determination of absolute nuclear position in the diamond lattice. However, direct comparison to the microscopic model depends sensitively on the details of the electronic wave function because of both the isotropic contact contribution and the averaged dipolar term in Eq. 1. Our results indicate that both terms can be important. For example, although the point dipole approximation yields results that are qualitatively similar to experimental data, it underestimates the coherent coupling strength as well as the echo collapse rate. At the same time, fits for NV centers D and E (Fig. 4, B to D, solid lines) indicate that some amount of anisotropic dipolar contribution is present (*27*). In fact, these fits yield an estimate of the electron-spin density at the positions of the proximal nuclei (*27*); by analyzing such data from a sufficiently large number of individual NV centers, it may be possible to determine the electronic wavefunction. This intriguing problem warrants future investigation.

Beyond providing a detailed insight into the mesoscopic environment of the spin qubit, our observations demonstrate a previously unknown mechanism for selective addressing and manipulation of single, isolated nuclear spins, even at room temperature. For example, such nuclear spins could be used as a resource for long-term storage of quantum information. They can be effectively manipulated via nearby electronic spins and potentially coupled together to explore a variety of proposed quantum information systems (*11*, *21*).

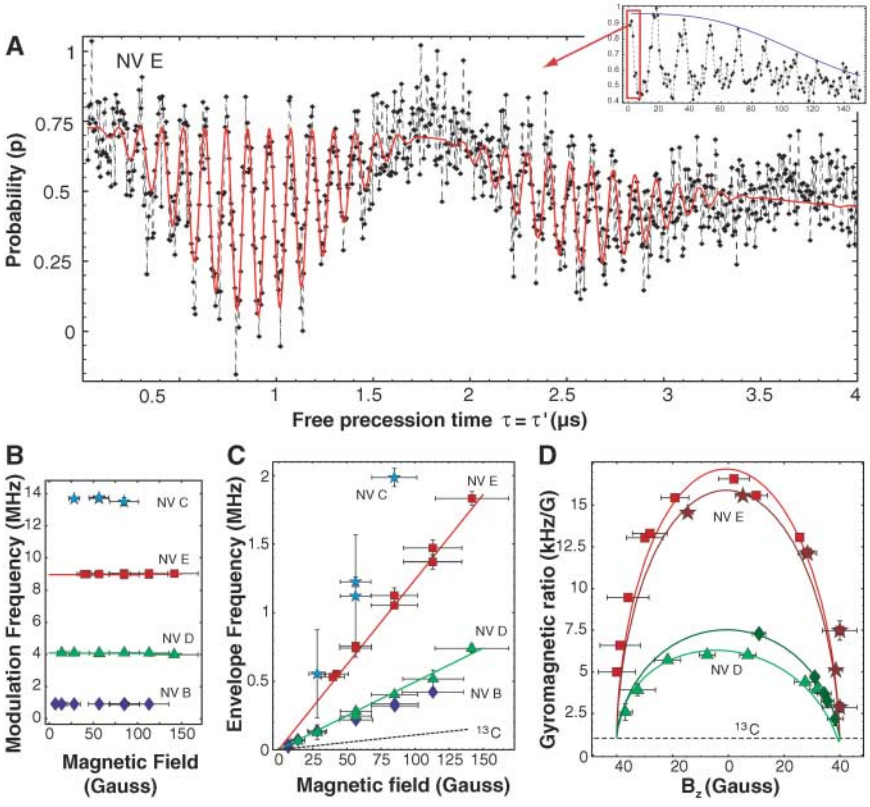

Fig. 4. (**A**) Spin-echo modulation as observed for NV E with B = 42 ± 6 G $\parallel -\hat{x} + \hat{z}$. The red curve represents a theoretical fit with the expected functional form $\exp[-(\tau/\tau_c)^4][a - b\sin(\omega_0\,\tau/2)^2\sin(\omega_1\,\tau/2)^2]$, yielding the modulation frequency $\omega_0 \sim 2\pi$ 9 MHz and envelope frequency $\omega_1 \sim 2\pi$ 0.6 MHz. (**B**) Modulation frequency for NV B to E as a function of magnetic field B $\parallel -\hat{x} + \hat{z}$. (**C**) Envelope frequency [same conditions as (B)]. The envelope frequencies are different for each center, but they all exceed the bare ^{13}C Larmor precession frequency (dashed line). (**D**) Effective gyromagnetic ratio (envelope frequency/magnetic field) versus magnetic field orientation for NV centers D and E. The amplitude of the magnetic field is fixed at 40 ± 4 G. The magnetic field is varied in the *xz* plane for NV center D (red boxes) and NV center E (green triangles) and *yz* plane for NV center D (dark red stars) and NV center E (dark green diamonds). Six free parameters that describe the interaction with the nearest ^{13}C spin were fit to the envelope and modulation frequency data (*27*), yielding the solid curves shown in (B) to (D). Error bars indicate a 95% confidence interval for fits to the data (*y* axis) and estimated error in magnetic field measurement (*x* axis) obtained from the discrepancy between Hall sensor measurements and the observed Zeeman splitting of the NV center.

References and Notes

1. D. P. DiVincenzo, *Science* **270**, 255 (1995).
2. F. Jelezko, T. Gaebel, I. Popa, A. Gruber, J. Wrachtrup, *Phys. Rev. Lett.* **92**, 076401 (2004).
3. F. Jelezko *et al.*, *Phys. Rev. Lett.* **92**, 130501 (2004).
4. F. Jelezko, J. Wrachtrup, *J. Phys. Condens. Matter* **16**, R1089 (2004).
5. R. J. Epstein, F. Mendoza, Y. K. Kato, D. D. Awschalom, *Nat. Phys.* **1**, 94 (2005).
6. R. Hanson, F. M. Mendoza, R. J. Epstein, D. D. Awschalom, *Phys. Rev. Lett.* **97**, 087601 (2006).
7. X. Li *et al.*, *Science* **301**, 809 (2003).
8. F. H. L. Koppens *et al.*, *Science* **309**, 1346 (2005); published online 21 July 2005 (10.1126/science.1113719).
9. J. R. Petta *et al.*, *Science* **309**, 2180 (2005); published online 1 September 2005 (10.1126/science.1116955).
10. M. Atature *et al.*, *Science* **312**, 551 (2006); published online 5 April 2006 (10.1126/science.1126074).
11. B. E. Kane, *Nature* **393**, 133 (1998).
12. R. G. Clark *et al.*, *Philos. Trans. Royal Soc. A* **361**, 1451 (2003).
13. Y. Makhlin, G. Schon, A. Shnirman, *Rev. Mod. Phys.* **73**, 357 (2001).
14. J. I. Cirac, P. Zoller, *Phys. Today* **57**, 38 (2004).
15. A. V. Khaetskii, D. Loss, L. Glazman, *Phys. Rev. Lett.* **88**, 186802 (2002).
16. J. Schliemann, A. Khaetskii, D. Loss, *J. Phys. Cond. Matter* **15**, R1809 (2003).
17. N. Shenvi, R. de Sousa, K. B. Whaley, *Phys. Rev. B* **71**, 144419 (2005).
18. R. de Sousa, S. Das Sarma, *Phys. Rev. B* **68**, 115322 (2003).
19. W. Yao, R. Liu, L. J. Sham, http://arxiv.org/abs/cond-mat?papernum=0508441 (2005).
20. T. D. Ladd *et al.*, *Phys. Rev. B* **71**, 014401 (2005).
21. L. Childress, J. M. Taylor, A. S. Sørensen, M. D. Lukin, *Phys. Rev. Lett.* **96**, 070504 (2006).
22. P. van Loock *et al.*, *Phys. Rev. Lett.* **96**, 240501 (2006).
23. A. Schweiger, G. Jeschke, *Principles of Pulse Electron Paramagnetic Resonance* (Oxford Univ. Press, Oxford, 2001).
24. T. Gaebel *et al.*, *Nat. Phys.* **2**, 408 (2006).
25. A. Szabo, T. Muramoto, R. Kaarli, *Phys. Rev. B* **42**, 7769 (1990).

26. L. G. Rowan, E. L. Hahn, W. B. Mims, *Phys. Rev.* **137**, A61 (1965).
27. Materials and methods are available on *Science* Online.
28. M. O. Scully, M. S. Zubairy, *Quantum Optics* (Cambridge Univ. Press, Cambridge, 1997).
29. E. L. Hahn, *Phys. Rev.* **80**, 580 (1950).
30. E. van Oort, M. Glasbeek, *Chem. Phys.* **143**, 131 (1990).
31. C. P. Slichter, *Principles of Magnetic Resonance* (Springer-Verlag, New York, 1990).

32. We are grateful to J. Doyle and Doyle lab members for making these experiments possible. We thank A. Mukherjee, N. Khaneja, E. Demler, C. Marcus, and S. Sachdev for many stimulating discussions and experimental help and S. Prawer for providing high-purity diamond samples. This work was supported in part by the NSF Career Award; Army Research Office Multidisciplinary University Research Initiative; and the Packard, Sloan, and Hertz Foundations. F.J. and J.W. acknowledge support from Deutschen Forschungsgemeinschaft (SFB/TR21) and the European Commission (Q.A.P.).

Supporting Online Material
www.sciencemag.org/cgi/content/full/1131871/DC1
Materials and Methods
References

28 June 2006; accepted 23 August 2006
Published online 14 September 2006;
10.1126/science.1131871
Include this information when citing this paper.

Rapid Early Development of Circumarctic Peatlands and Atmospheric CH_4 and CO_2 Variations

Glen M. MacDonald,[1,2]* David W. Beilman,[1] Konstantine V. Kremenetski,[1,3] Yongwei Sheng,[1] Laurence C. Smith,[1] Andrei A. Velichko[3]

An analysis of 1516 radiocarbon dates demonstrates that the development of the current circumarctic peatlands began ~16.5 thousand years ago (ka) and expanded explosively between 12 and 8 ka in concert with high summer insolation and increasing temperatures. Their rapid development contributed to the sustained peak in CH_4 and modest decline of CO_2 during the early Holocene and likely contributed to CH_4 and CO_2 fluctuations during earlier interglacial and interstadial transitions. Given the decreased tempo of peatland initiation in the late Holocene and the transition of many from fens (which generated high levels of CH_4) to ombrotrophic bogs, a neoglacial expansion of northern peatlands cannot explain the increase in atmospheric CH_4 that occurred after 6 ka.

Modern northern peatlands cover about 4 million km² across Eurasia and North America and represent the biggest wetland complex in the world (Fig. 1). Today, these peatlands are thought to store 180 to 455 Pg of sequestered carbon while also releasing 20 to 45 Tg per year of CH_4 into the atmosphere (*1*, *2*). The potential contribution of northern peatlands to fluctuations in atmospheric CH_4 and CO_2 over the late glacial and Holocene, and during earlier interglacials, has been a matter of much speculation and debate (*3*–*8*).

Ice-core records show that CH_4 concentrations rose from ~350 to 650 parts per billion by volume (ppbv) between the last glacial maximum (LGM), which occurred 20 ka (20,000 calendar years before C.E. 1950), and the Bølling-Allerød (BA) warm period (~15 to 13 ka). They then declined by ~200 ppbv during the Younger Dryas (YD) stadial (~13 to 11.5 ka), rose rapidly to levels over 700 ppbv in the early Holocene (11 to 8 ka), and then declined again between 8 and 6 ka (*3*). It has been maintained that because conditions were not favorable for widespread circumarctic peatland formation until after 8 ka, tropical wetlands or marine clathrates were the likely sources for the CH_4 peak that occurred 11 to 8 ka (*4*, *9*). On the basis of the assumed late-Holocene development, it has been suggested that northern peatlands played little role in the declining atmospheric CO_2, which has also been observed during the period from 11 to 8 ka (*5*). Others argue that the development of the northern peatland complex contributed substantially to the early-Holocene CH_4 increase and simultaneously decreased atmospheric CO_2 through carbon sequestration in northern soils (*6*–*8*).

Resolving the debate on the potential role of the northern peatlands in early postglacial CH_4 variations has become critical since the recent analysis of the deuterium and carbon isotopic composition of CH_4 (δD_{CH_4} and $\delta^{13}C_{CH_4}$) from Greenland ice samples, which suggested that the destabilization of marine clathrates is an unlikely explanation for the BA or early-Holocene CH_4 increases (*10*, *11*). In view of this evidence, it has been argued that the sustained high levels of CH_4 that developed at the close of the YD in part require a persistent terrestrial source linked to the warming climate at that time (*11*).

Holocene concentrations of atmospheric CH_4 reached a minimum of <600 ppbv at 6 ka and then increased again over the late Holocene to values of about 695 ppbv just before the industrial revolution (*3*). This late-Holocene increase has been variously attributed either to expansion of northern wetlands due to neoglacial climatic cooling after the Holocene thermal maximum (*4*) or to the product of expanding anthropogenic activity (particularly the expansion of rice- and cattle-based agrarian societies) in the mid- to late Holocene (*12*). However, recently collected CH_4 data from Antarctic ice cores reveal that the mid- to late-Holocene increase is not unique. A similar late-interglacial increase in Pleistocene atmospheric CH_4 occurred ~400 ka during Marine Isotope Stage 11 (MIS11), which clearly cannot reflect anthropogenic sources and has been ascribed instead to natural factors, including expansion of northern wetlands (*13*).

To address the hypothesis that northern peatland development could have contributed to the late-Pleistocene and Holocene variations in atmospheric CH_4 and CO_2 outlined above, we collated 1516 basal radiocarbon dates for peat initiation from wetlands throughout high-latitude Europe, Asia, and North America from a wide variety of sources (*14*). Some areas, such as Fennoscandia, have numerous basal dates for a small geographic area, whereas other very large areas such as central and eastern Siberia have a limited number of dates (Fig. 1). Therefore, we analyzed the compiled data set by raw number of initiation dates, and we also divided the Northern Hemisphere into grids of 2° latitude by 2° longitude and assigned a value for peatland initiation based on the oldest basal radiocarbon date in each cell (Fig. 1).

The lack of basal dates older than about 16.5 ka suggests that there was no extensive peatland complex in the northern circumpolar region during the LGM (Fig. 2). This finding is corroborated by palynological data that indicate a paucity of *Sphagnum* (peat moss) spores from deposits of this age (*15*). Before 16.5 ka, much of the North American and European arctic and subarctic were still covered in ice, and it is likely that the large ice-free areas of Siberia and Beringia were too cold and dry (*16*) to promote extensive peatland development. This absence of any significant northern peatland complex during the LGM is consistent with the depressed CH_4 levels and the relatively low proportion of northern CH_4 sources observed in ice-core records (Fig. 3).

In concert with increasing summer insolation and northern high-latitude temperatures, the current northern peatland complex began developing in ice-free portions of North America and Asia between 16.5 and 14 ka and initiating widely on all three northern continents after 14 ka (Figs. 1 and 2). These results dispel the earlier assertion that peatland development in

[1]Department of Geography, [2]Department of Ecology and Evolutionary Biology, University of California, Los Angeles, CA 90095–1524, USA. [3]Russian Academy of Sciences, Moscow 109017, Russia.

*To whom correspondence should be addressed. E-mail: macdonal@geog.ucla.edu